

Compact In-Band Full-Duplex Implantable Antenna for Wireless Capsule Endoscopy

Abdullah Alshammari, *Student Member, IEEE*, Amjad Iqbal, *Member, IEEE*, Abdul Basir, *Member, IEEE*, Muath Al-Hasan, *Senior Member IEEE*, Roy B. V. B. Simorangkir, *Member, IEEE*, Mourad Nedil, *Senior Member, IEEE*, Ismail Ben Mabrouk, *Senior Member, IEEE*

Abstract—This study presents an ultra-miniaturized implantable in-band full-duplex (IBFD) antenna, designed for wireless capsule endoscopy (WCE) applications. Through the integration of semi-circular slots and shorting pins, the antenna achieves a small volume of 7.17 mm^3 ($\pi \times (3 \text{ mm})^2 \times 0.254 \text{ mm}$), surpassing the state-of-the-art in compactness. Simulations of the proposed design are conducted within a human body phantom to demonstrate the antenna's operation at 2.45 GHz. Radiation patterns from both ports are nearly omnidirectional, and an isolation level of greater than 28 dB is achieved. Our results indicate that the antenna can establish reliable wireless communication over distances exceeding 8 meters, with a 10 dB margin at both ports. The specific absorption rate (SAR) values at 2.45 GHz is found to be 29.7 W/kg at 1W input power. Experimental validation using minced pork demonstrated a good agreement with simulation results.

Index Terms—In Band Full-Duplex, Implantable Antenna, Medical Implants, wireless capsule endoscopy.

I. INTRODUCTION

WIRELESS capsule endoscopy (WCE) has revolutionized gastrointestinal diagnostics, offering a minimally invasive, patient-friendly alternative to traditional endoscopy methods. However, the increasing demand for miniaturized devices pose significant challenges in developing implantable antennas for such systems [1]–[3]. These antennas must be capable of efficiently transmitting and receiving electromagnetic waves through the complex propagation environments of the human body while maintaining a compact structure. To achieve such a compact size, various techniques have been employed to achieve size reduction, including the use of high permittivity laminates [4], capacitive slots [5], inductive stubs [6], defected ground planes [7], shorting pins [8], and slow wave structures [9]. In [10] significant size reductions have been achieved by increasing the current path with embedded meandered slots

and ground plane slots. A meandered resonator and an open-ended slot in the ground plane have been used to achieve an ultra-compact antenna design with a total volume of 21 mm^3 [11]. In [12], the authors have proposed a magnetostrictive antenna that can operate at a low MHz frequency range inside the human body. In [13], an optimized antenna structure that fits within the limited space of WCE devices is presented. The miniaturization technique includes slots and shorting pins that effectively reduce the antenna size while maintaining its functionality. Similarly, the study in [14] demonstrates how the size of an antenna operating at 915 MHz and 2450 MHz can be minimized by incorporating slots into both the patch and the ground plane. Moreover, the research presented in [15] introduces a low-profile antenna developed using shorting pins combined with circular and open-ended slots. However, such miniaturization techniques can adversely impact antenna performance resulting in increased design complexity and lower peak gains, limiting their integration with most Implantable Medical Devices (IMDs).

The antennas mentioned above have good performances in terms of size and radiation characteristics. However, their one-port configuration restrict them from simultaneous transmission and reception without an internal multiplexer. In fact, these antennas can either be used for transmission or reception. In order to use them for simultaneous transmission and reception, they must be integrated with a highly-isolated multiplexer. This integration increases the system's size, complexity, and power consumption. Consequently, designing compact, power-efficient wireless implantable devices becomes significantly more challenging. Recent studies in [16] and [17] have proposed the use of duplexing antennas to overcome the limitations associated with the size and complexity of biomedical implants. In [16], a self-duplexing antenna, operating at 915 and 1470 MHz, is designed for multi-tasking biomedical implants. It occupies a total volume of 9.4 mm^3 and maintains an isolation level better than 21 dB. In [17], the authors have developed a full-duplex implantable antenna that operates at both 915 MHz and 1300 MHz. The 915 MHz frequency band is dedicated to biotelemetry, while the 1300 MHz frequency band is utilized for wireless power transmission. The full duplex antenna has a total volume of 8.32 mm^3 and maintains a better isolation level. Despite their ability to communicate simultaneously without a multiplexer, this approach leads to less efficient spectrum utilization due to the use of multiple frequency bands. Additionally, this method may encounter increased interference from neighboring de-

Manuscript received —. This work was supported by the Royal Society under Newton International Fellowship (Grant Number: NIF\R1\221500) (Corresponding author: Amjad Iqbal).

Abdullah Alshammari, Amjad Iqbal, Roy B. V. B. Simorangkir and Ismail Ben Mabrouk are with the Department of Engineering, Durham University, Durham DH1 3LE, U.K. (e-mail: Abdullah.alshammari@durham.ac.uk; amjad730@gmail.com; roy.b.simorangkir@durham.ac.uk; ismail.benmabrouk@durham.ac.uk).

A. Basir is with the Faculty of Information Technology and Communication Sciences, Tampere University, Finland (Email: abdul.basir@tuni.fi).

Muath Al-Hasan is with the Network and Communications Engineering Department, Al Ain University, Al Ain, United Arab Emirates (e-mail: muath.alhasan@aau.ac.ae).

Mourad Nedil is with the Communications Research Laboratory, University of Quebec at Abitibi-Temiscamingue, Val-d'Or, QC J9P 1Y3, Canada (e-mail: Mourad.Nedil@uqat.ca)

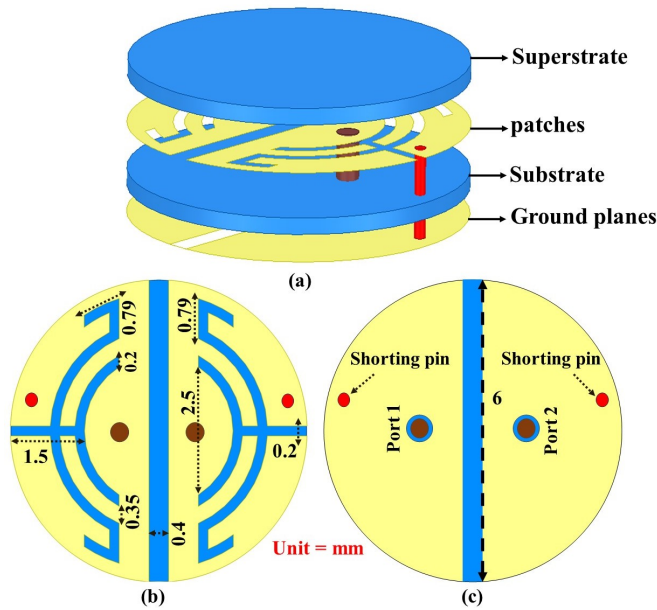


Fig. 1. Proposed antenna (a) Exploded view of the structure of the antenna. (b) Top view. (c) Bottom view.

vices operating on adjacent frequency bands [18]–[20].

To address the challenges discussed above, this paper introduces the first in-band full-duplex (IBFD) antenna designed for WCE. In-band duplexing systems can simultaneously transmit (Tx) and receive (Rx) signals in the same frequency band without requiring an external multiplexer. The proposed IBFD antenna features an ultra-compact size of only 7.17 mm³ including a semi-circular slot and shorting pins. This innovative design marks a significant advancement in IMDs technology, offering a miniaturized design and minimum self-interference while maintaining high performance at the 2.45 GHz ISM band.

II. IN-BAND FULL-DUPLEX ANTENNA DESIGN

The proposed IBFD antenna comprises two identical semi-circular patches and two separate semi-circular ground planes, as illustrated in Fig. 1. The superstrate and substrate are made from Rogers RT/duroid 5880 material with a dielectric constant of $\epsilon_r = 2.2$, $\tan\delta = 0.003$, and a thickness of 0.254 mm. To minimise the proposed IBFD antenna size, multiple semi-circular and open-ended slots are incorporated in both radiating patches. Additionally, shorting pins have been inserted between the patches and the ground planes to achieve further compactness. The two patches have no direct connection, so as for the ground planes. Thus, power from one patch cannot directly travel to the other patch. However, there is still a coupling between the two patches due to the fringing fields between them. A gap with a width of 0.4 mm is inserted between the two patches to minimize mutual coupling. Increasing the gap width between the patches improves isolation. However, it also increases the antenna's overall dimensions. Therefore, a proper gap of 0.4 mm is maintained between both patches and ground planes to ensure high isolation level while maintaining a compact size. A capsule shell made from Polylactic Acid (PLA) material, with

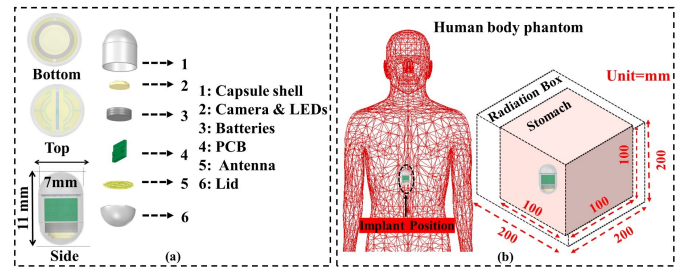


Fig. 2. (a) Architecture of the capsule device. (b) Simulation scenarios for the antenna.

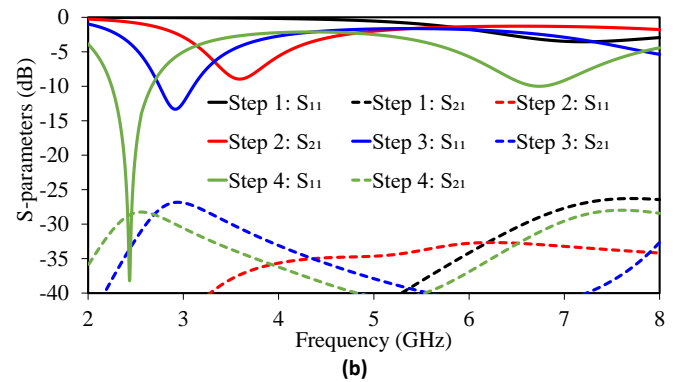
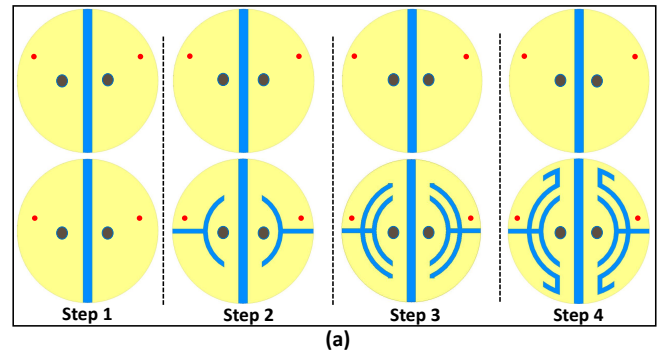


Fig. 3. (a) Antenna evolution stages (design steps). (b) Design step results.

relative permittivity (ϵ_r) of 2.8 and a thickness of 0.2 mm is used to encase the implantable antenna. The length of the capsule shell is 11 mm, and the radius is 3.5 mm. The capsule is composed of electronic components, such as a printed circuit board (PCB), batteries, sensors, light-emitting diodes (LEDs), and a camera, as shown in Fig. 2 (a). The suggested design is simulated within the stomach of a human body phantom, as shown in Fig. 2 (b).

A. Simulation Environment

The design and simulation processes are conducted using Ansys HFSS electromagnetic software. The antenna design is tested using a model representing the human stomach, as shown in Fig. 2(b). The simulations are performed in two steps in order to save simulation time. First, the antenna is simulated in a simple stomach model (homogeneous box) that measures 100 × 100 × 100 mm³. This basic model is used because it has properties similar to real stomach tissues. The electrical properties of a human stomach are listed in Table I [21]. The proposed antenna is placed 50 mm deep in the model in this

TABLE I.
STOMACH TISSUE PROPERTIES AT 2.45 GHz

| Tissue name | Frequency (GHz) | Conductivity (S/m) | Relative permittivity | Loss tangent |
|-------------|-----------------|--------------------|-----------------------|--------------|
| Stomach | 2.45 | 2.2105 | 62.158 | 0.26092 |

phase. Second, the antenna is fine-tuned using a more detailed human body model (implantation depth = 50 mm). The human model is placed within a cubic radiation box measuring $800 \times 800 \times 800 \text{ mm}^3$. The dimensions ensure that the box extends at least a quarter wavelength ($\lambda/4$) from the antenna, providing sufficient space for accurate radiation pattern analysis.

B. Design Evolution

The design process of the proposed duplex antenna is illustrated in Fig. 3(a). The S-parameters (reflection (S_{11} , S_{22}) and transmission (S_{21}) coefficients) of each step are shown in Fig. 3(b). The antenna structure is modified during the design process to achieve a compact geometry, and high isolation. In all design steps, the position of the coaxial feeding cables remains unchanged. The design process is completed in four steps, as described below:

Step 1: The design process is started by drafting a circular patch and a ground plane over the substrate, followed by splitting them into semi-circular shapes (two semicircular patches and two semicircular groundplanes). In Step 1, the gap between both patches and both ground planes is maintained at 0.4 mm to achieve a better isolation level. Shorting pins are added to both radiators to further minimize the antenna's dimensions. These modifications are implemented by drilling through the substrate to establish a conductive path between the patch and the ground plane, as depicted in Fig. 3(a). In fact, adding a shorting pin generates additional inductance, which ultimately reduces the overall geometry of the antenna through reducing the resonance frequency of the antenna [22]. As a result of these modifications in conventional circular patch antenna, the semi-circular patch (in Step 1) resonates at 7 GHz, as illustrated in Fig. 3(b). It can be observed that the proposed semicircular patches exhibits poor matching in this step. The matching can be enhanced by changing the position of the excitation ports. However, the main objective of this work is to achieve enough compactness. In addition, our desired frequency is 2.45 GHz, which is far lower than 7 GHz. Furthermore, the reflection coefficients of both patches are the same due to the exact symmetry.

Step 2: In Step 2, as depicted in Fig. 3(a), the size of the antenna is further reduced by shifting the resonant frequency to the lower band. This step involves adding open-ended and semi-circular slots to both patches. The addition of these slots generates additional capacitance, which shifts the resonant frequency to the lower band. As a result of such modifications in this step, the antenna now resonates at 3.6 GHz, attaining a compactness of 48.57% compared to Step 1. In this step, the isolation level between both patches is better than 26 dB, as displayed in Fig. 3(b).

Step 3: In Step 3, the semicircular patch is further modified by adding one additional semi-circular slot, lowering the

resonant frequency from 3.6 GHz to 2.9 GHz. This is because the additional slot adds more capacitance to the equivalent capacitance of the antenna. In addition, this design maintains an isolation level better than 26 dB. As a result of the additional semi-circular slot, a compactness of 58.57% is achieved compared to Step 1. The configuration in Step 3 has yet to align successfully with the target operational frequency of 2.45 GHz.

Step 4: In Step 4, small arc-shaped slots are added on either side of the larger semi-circular slot to bring the resonant frequency to the targeted 2.45 GHz band. With this approach, a size reduction of 65% is obtained compared to Step 1. This design maintains an isolation level better than 28 dB within the operational bandwidth.

C. Parametric Analysis

The proposed antenna configuration provides the distinct capability to adjust its resonant frequency. A detailed parametric study is carried out to fine-tune various essential parameters. This process involves changing a single parameter while keeping the rest of the parameters at their optimum values.

1) *Effect of Slot Length (a)*: Slots are incorporated into the radiating patch to reduce the overall dimensions of the antenna. The slot length is varied from 0.25 mm to 0.79 mm to investigate its effect on the resonant frequency. This analysis found that extending the slot length results in a frequency shift from 2.63 GHz to 2.45 GHz. This shift shows the critical role of slot dimensions in adjusting the resonant frequency, contributing to the miniaturization process.

2) *Open-ended slot Length (L)*: The miniaturization of the antenna is mainly caused by the slots on the patch, including the open-ended slot. To investigate the impact of the open-ended slot length (L) on the reflection coefficient, a series of simulations are performed by varying the length from 1 mm to 1.5 mm. Consequently, the resonant frequency band is shifted from 2.6 GHz to 2.45 GHz. In fact, introducing open-ended slots in the radiating patch increases the current path, and thus, lowering the resonance frequency.

3) *Antenna coupling with other components of the WCE*: Considering the WCE device, it's crucial to carefully assess the proximity of the antenna to the internal PCB and surface-mounted devices. The electromagnetic coupling between the antenna with other parts of the device may affect the antenna parameters. The typical WCE components include a series of surface-mounted electronic parts, PCB, LEDs, cameras, and batteries, with the PCB often being in close proximity to the antenna. A detailed parametric study was conducted to carefully evaluate the influence of the PCB and associated electronic components on the IBFD antenna's performance. This investigation aimed to determine the optimal gap between the antenna and internal circuitry in order to mitigate any unwanted effects on the antenna's reflection coefficient. The results demonstrate that changes in the "Gap" exert minimal impact on the reflection coefficient compared to the isolation level, indicating a robust design that is resilient to minor changes in positioning. The analysis shows that the gap

between the antenna and electronic components has negligible influence on the isolation level. This is because the primary coupling mechanisms responsible for self-interference, such as surface wave coupling through the substrate and near-field coupling above the antenna, are not significantly affected by the gap between the antenna and PCB [23], [24]. Consequently, the antenna is placed with a Gap of 1 mm from the PCB to ensure optimal performance within the spatial constraints of the WCE device.

D. Effect of G_1 (the gap between the patches) and G_2 (the gap between the grounds) on the S-parameters

The two patches have no direct connection, so as for the ground planes. Thus, power from one patch cannot directly travel to the other patch. However, there is still a coupling between the two patches due to the fringing fields between them. Increasing the gap width between the patches improves isolation. However, it also increases the antenna's overall dimensions. A parametric analysis was conducted to examine the impact of G_1 (the gap between the patches) and G_2 (the gap between the grounds) on the isolation level. The results indicate that as G_1 and G_2 increase, the isolation level improves. This improvement is attributed to the fact that larger gaps (G_1 and G_2) reduce capacitive coupling, thereby enhancing isolation.

III. ANTENNA PERFORMANCE AND DISCUSSION

This section provides a comprehensive examination of the proposed IBFD antenna's performance, focusing on key aspects such as S-parameters, radiation patterns, SAR, current distribution, and link budget. The simulated results are obtained with the antenna placed in the stomach of the human torso model. To validate the simulated results and ensure the desired performance, the antenna is fabricated and subjected to a series of measurements. Coaxial cables are carefully soldered to each patch of the fabricated prototype to facilitate testing. As depicted in Fig. 4(a), the proposed IBFD antenna is then integrated into a WCE device along with batteries and a printed circuit board. The capsule shell is made of 3D-printed polylactic acid (PLA) for biocompatibility and structural integrity. Upon assembly, the capsule is sealed with epoxy to ensure durability and maintain its integrity. To evaluate the antenna's performance under conditions that closely resemble the human gastrointestinal tract, the assembled WCE device is placed in a container filled with minced pork at a depth of approximately 50 mm, as shown in Fig. 4(b) and (c).

A. S-Parameters

The antenna's S-parameters is measured using a P9374A vector Network Analyzer (VNA) from Keysight. As shown in Fig. 5, the simulated results demonstrate consistent resonant behaviors at 2.45 GHz for both S_{11} and S_{22} , exhibiting a 10 dB-return loss bandwidth of 400 MHz. The measured results, however, show a slight shift in the resonant frequency to around 2.4 GHz with a 10 dB-return loss bandwidths of 170 MHz and 330 MHz for S_{11} and S_{22} , respectively. The isolation

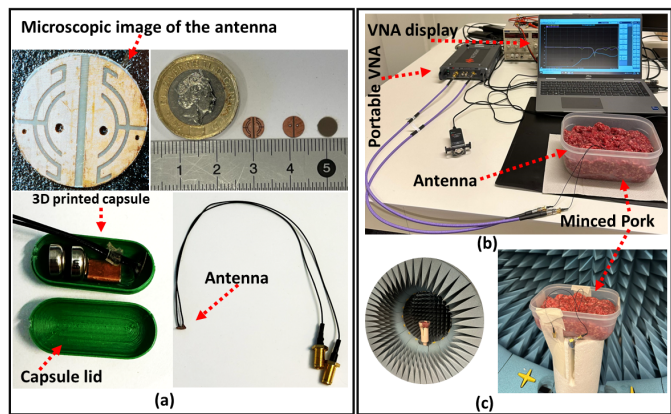


Fig. 4. (a) Fabricated antenna prototype before and after integration into WCE. Measurement setups: (b) S-parameters and (c) radiation patterns.

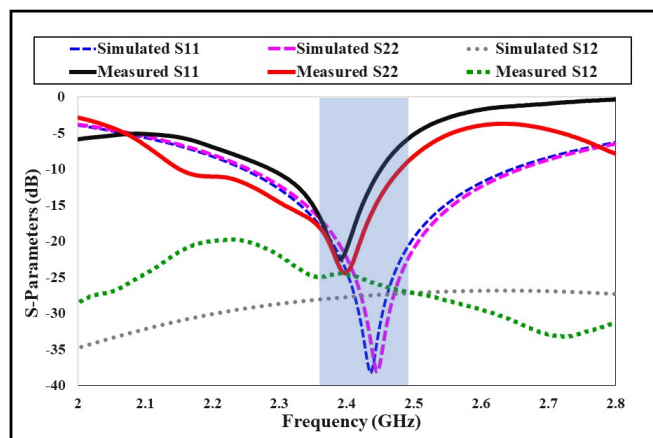


Fig. 5. Simulated and measured S-parameters of the proposed antenna.

between the ports is better than 28 dB in both simulated and measured results. The discrepancies between the simulated and measured S-parameter results can be attributed to several factors. One contributing factor is the potential variation in the dielectric properties of the phantom material used in the simulations compared to the actual minced pork used in the measurements. Another factor is related to the assembly of the antenna within the WCE device. The presence of components inside the capsule and the antenna positioning relative to these components may differ from the ideal simulation scenario. Additionally, the connection of the coaxial cables to the antenna ports through soldering may also introduce parasitic capacitances and inductances, which can contribute to such variations. Despite these discrepancies, the antenna still maintains satisfactory return loss and isolation characteristics, validating the design and its potential for the targetted WCE applications.

B. Radiation Patterns and Gain

Fig. 6 displays the measured and simulated radiation patterns of the proposed antenna at 2.45 GHz when excited through ports 1 and 2 separately. The simulation results were obtained by placing the antenna in the stomach of the human body model. The measurements were conducted in an

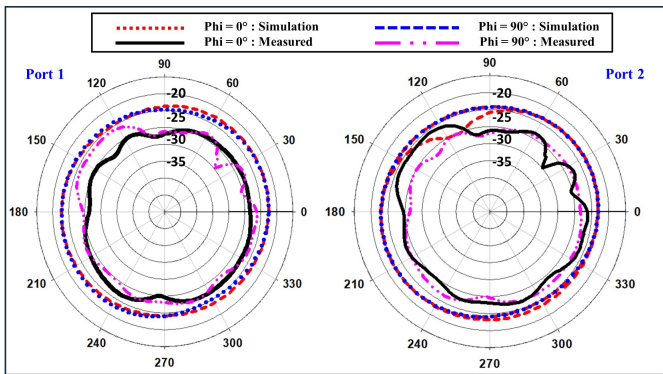


Fig. 6. Simulated and measured radiation patterns of the proposed antenna at 2.45 GHz.

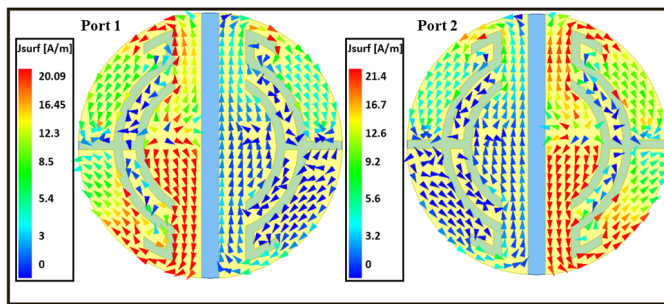


Fig. 7. Antenna current distributions at 2.45 GHz when fed through port 1 and 2 individually.

anechoic chamber. The capsule device containing the antenna is positioned at the center of the minced pork container and the receiving antenna is placed at a distance of 1 meter from the container, ensuring far-field conditions. The radiation patterns are obtained by rotating the capsule device in increments of 2 degrees while keeping the receiving antenna stationary. During the measurements, one port of the antenna is terminated with a 50Ω load, while the other is connected to a spectrum analyzer. As evident from Fig. 6, some discrepancies can be observed between the simulated and measured patterns, particularly in terms of the peak realized gain values. The simulated peak realized gains are -24.4 dB and -24.5 dB for ports 1 and 2, respectively. In contrast, the measured peak realized gains are -30.26 dB and -31.5 dB. The lower gain values in the measurements can be an indication of the higher losses associated with the minced pork compared to the simulated human tissue phantom model. Despite the differences in peak realized gain, the overall characteristics of the radiation patterns remain consistent between the simulated and measured results. The antenna exhibits omnidirectional radiation performance, which is crucial for maintaining reliable communication links regardless of the antenna's orientation within the gastrointestinal tract [25], [26].

C. Current distribution

Fig. 7 illustrates the surface current distributions on the IBFD antenna's patches when activating Ports 1 and 2 separately. With Port 1 active and Port 2 matched, the currents concentrate around the feed point and extend towards the semi-circular slots on the active patch. This pattern reveals the wave

TABLE II.
Calculated Peak SAR (1 W Input Power) and Corresponding Allowable Maximum Input Powers

| Frequency (GHz) | Phantom type | SAR (W/kg) | | Max allowable power (mW) | |
|-----------------|--------------|------------|------|--------------------------|-------|
| | | 1-g | 10-g | 1-g | 10-g |
| 2.45 | Human Body | 274.6 | 29.7 | 5.82 | 67.34 |

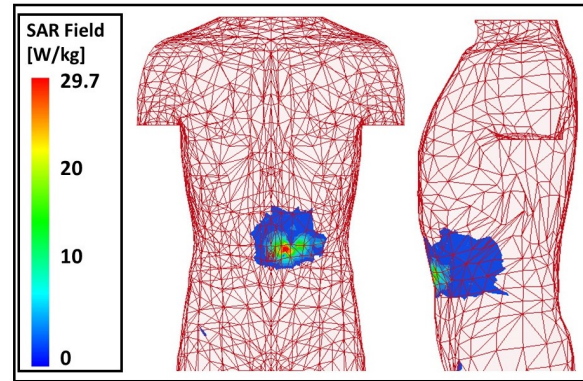


Fig. 8. SAR distributions at 2.45 GHz over 10-g tissue when each port is powered individually with 1 W.

propagation path and highlights the design's effectiveness in confining currents to the active patch, enhancing port isolation. The semi-circular slots play a crucial role in lengthening the current path, effectively increasing the electrical length of the patch without altering its physical size. This technique enables a more compact antenna design while maintaining the desired operating frequency. Moreover, the slots help confine the currents to the active patch, minimizing leakage to the inactive patch and achieving high isolation between ports. Similarly, when Port 2 is activated, the current distribution remains primarily within the intended patch, demonstrating the antenna's consistent performance in maintaining high isolation levels under different operating conditions. The inactive regions exhibit significantly lower current densities compared to the active areas, further validating the design's effectiveness in achieving high isolation between the radiating elements.

D. SAR

Ensuring the safety of patients is of utmost importance when designing and utilizing implantable WCE devices. The SAR is a crucial metric that quantifies the energy absorbed by human tissues from the electromagnetic fields generated by the antenna. The updated IEEE C95.1-2019 standard requires that the maximum 10-g averaged SAR value should not exceed 2 W/kg [27]. To assess the SAR of the proposed antenna, a human torso phantom with the implanted capsule, as illustrated in Fig. 8, is employed in the simulations. Comprehensive SAR evaluations are conducted by applying an input power of 1 W to each antenna port separately. The computed peak SAR values at the operating frequency of 2.45 GHz are summarized in Table II, which includes both 1-g and 10-g averaged SAR values. The 1-g SAR values are provided to enable comparisons with previous studies. The simulation results reveal that

TABLE III.
Link margin Parameters

| Specification | Variable | Value |
|--------------------------------|-------------|---------------------|
| Resonant frequency (GHz) | f | 2.45 |
| Transmitter Power (dBm) | P_a | -16 |
| Path loss exponent | γ | 1.5 |
| Temperature (Kelvin) | T | 273 |
| Transmitter antenna gain (dBi) | G_a | -24.4 /-24.5 |
| Receiving antenna gain (dBi) | G_b | 2 |
| Free space loss (dB) | L | Distance dependent |
| Available power (dB) | A_p | Distance dependent |
| Required power (dB) | R_p | Adaptive (Bit rate) |
| Margin (dB) | $A_p - R_p$ | Fig.9 |

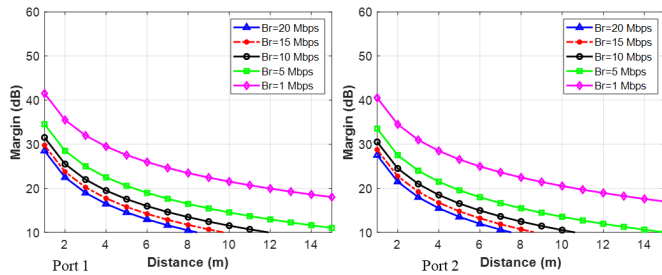


Fig. 9. Link margin of the proposed antenna.

the maximum 10-g averaged SAR values when the antenna is excited through ports 1 and 2 independently, are 29.7 W/kg, respectively. Although these values exceed the 2 W/kg limit, it is essential to emphasize that these measurements correspond to an input power of 1 W, which is significantly higher than the typical power levels used in WCE applications. To ensure compliance with the SAR safety guidelines, the maximum permissible input powers for the proposed antenna are determined based on the simulated SAR values. These maximum allowable input powers are presented in Table II. The results indicate that to adhere to the 10-g SAR limit of 2 W/kg, the maximum input powers should be limited to 67.34 mW for ports 1 and 2, respectively. It is worth noting that the typical power used for implantable devices, as specified in the ITU-R SM.2153-8 standard [28], is much lower than these maximum permissible input powers. These presented results instill confidence in the suitability and safety of the proposed antenna for the intended WCE applications.

E. Link margin Analysis

To evaluate the antenna's performance in facilitating effective data transmission from the implant to the external data receiver, a comprehensive link budget analysis is conducted. This analysis takes into account various factors that influence the signal quality, including path loss, mismatches between antenna components, cable transmission losses, and shadowing effects. Ensuring a minimum link margin of 10 dB is

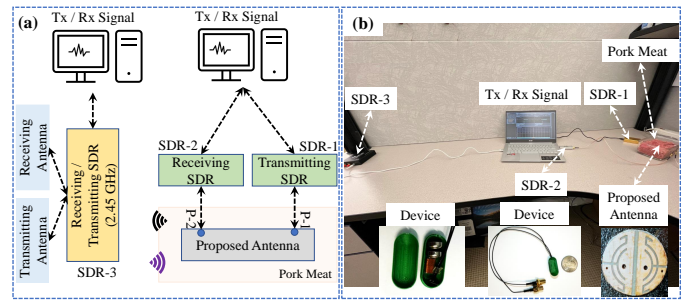


Fig. 10. Simultaneous uplink and downlink communication using the proposed in-band full-duplex antenna (a) block diagram, and (b) practical measurements.

crucial for maintaining reliable communication under diverse conditions [29]. The link budget analysis is performed using the Friis transmission formula, which predicts the antenna's capabilities in a given propagation environment [30]–[36]. The IBFD antenna served as the transmitter, operating at a power level of -16 dBm (25 μ W), while a dipole antenna acted as the receiver. The required receiver power (R_r) is calculated using the following equation:

$$R_r(\text{dB}) = \frac{E_b}{N_0} + KT + R_r \quad (1)$$

where R_r is the minimum power required at the receiver, T (293K) is the absolute temperature, E_b/N_0 is the energy-per-bit to noise power spectral density ratio (PSK modulation at 9.6 dB), K is the Boltzmann constant (1.38×10^{-23} J/K), and B_r is the bit rate. The available power (R_a) at the receiver is determined using:

$$R_a(\text{dB}) = P_t + G_t + G_r - L_{PL} - L_p \quad (2)$$

where P_t is the transmitted power, G_t and G_r are the transmitter and receiver antenna gains, L_{PL} the polarization loss, and L_p the path loss. The path loss (L_p) in the propagation environment is calculated using the log-distance path loss model:

$$L_p(\text{dB}) = 20 \log_{10} \left(\frac{4\pi d}{\lambda} \right) + 10\gamma \log_{10} \left(\frac{d}{d_0} \right) + S_e \quad (3)$$

Here, d is the distance between the antennas, λ the wavelength, γ the path loss exponent, and S_e the shadowing effect with a standard deviation σ .

The link budget analysis is performed at a fixed frequency of 2.45 GHz for both ports, considering data rates ranging from 1 to 20 Mbps. Fig. 9 presents the achieved link margins for these data rates, while Table III summarizes the essential parameters used in the analysis. The results demonstrate that the antenna consistently maintains a link margin of at least 10 dB, enabling reliable communication over distances exceeding 8 meters. Notably, even at the higher data rate of 20 Mbps, the effective communication range extends beyond 7 meters for both ports. These findings highlight the antenna's robustness in handling high data rate transmissions, making it suitable for biotelemetry applications in realistic biomedical scenarios.

TABLE IV. Comparison with State-of-the-Art Implantable Antennas (*Displays SAR Results For 1-gram Tissues, NG: Not given).

| Ref [] | [6] | [18] | [30] | [32] | [33] | [34] | [35] | [36] | This work |
|---------------------------------------|---------------------|--------------------|------------------------|------------------------|-------------------|------------------------|------------------------|----------------------|-----------------------------------------|
| Size (mm ³) | 6×6×2.54 = 91.44 | 1.4×10×10 = 140 | 8.8×8.8×4.8 = 371.7 | 7×6.5×0.377 = 17.15 | 32×10×0.2 = 64 | 17.25×8×0.6 = 87.63 | 22×23×1.27 = 642.62 | 5×5×0.635 = 15.87 | $\pi \times (3)^2 \times 0.2$ = 7.17 |
| Frequencies (GHz) | 0.9/2.45 | 0.4/2.4/5.7 | 1.4/2.45 | 0.402/1.6/2.45 | 0.402/0.9/2.4 | 0.433/0.915 | 0.402/2.45 | 1.4/2.45 | 2.45 |
| 10-g SAR (W/Kg) | 891/877* | 494/344/320* | NG | 92.7/85.3/81.7 | 316/358/247* | 179.7/160.7 | 832/690* | 81.7/84.6 | 29.7 |
| Gain (dBi) | -21/-19 | -45/-18/-14 | NG | -18.6/-18.4/-13.06 | -29.7/-28.7/-20.8 | -28.2/-24.5 | -36.7/-27.1 | -27.6/-27.1 | -24.4/-24.5 |
| Number of Ports | 1 | 1 | 1 | 1 | 1 | 1 | 1 | 1 | 2 |
| Isolation (dB) | ----- | ----- | ----- | ----- | ----- | ----- | ----- | ----- | >28 |
| Implant Depth (mm) | 45 | 3 | 12 | 3 | 100 | 100 | 4 | 62 | 50 |
| Simultaneous Transmission & Reception | No | No | No | No | No | No | No | No | Yes |
| External Multiplexer? | Yes | Yes | Yes | Yes | Yes | Yes | Yes | Yes | No |

F. Practical Demonstration of Simultaneous Uplink and Downlink Communication Ability

In this work, a compact in-band full-duplex (IBFD) antenna is designed and practically validated for wireless capsule endoscopy (WCE) applications. The main objective is to achieve simultaneous uplink and downlink wireless communication. To accomplish this, three software-defined radios (SDRs) are used. SDR-1 and SDR-2 are connected to the proposed IBFD antenna, while SDR-3 is connected to an external dipole antenna. Specifically, SDR-1 is connected to Port-1 (P-1) of the duplex antenna, and SDR-2 is connected to Port-2 (P-2) of the duplex antenna. Port-1 operates in transmitting mode, and Port-2 operates in receiving mode. SDR-3 is equipped with two dipole antennas (Dipole-3 and Dipole-4), where one antenna is in receiving mode and the other in transmitting mode. The block diagram of the overall setup is shown in Fig. 10. All SDRs are connected to a computer and operated using the open-source SDRangle software.

To investigate the self-interference phenomenon of the proposed duplex antenna, a narrow-frequency modulated (NFM) signal is transmitted through Port-1 of the duplex antenna using SDR-1. The same signal is observed through Port-2 of the duplex antenna using SDR-2. It is practically validated that minimal interference exists between the transmit and receive ports of the duplex antenna, as only a small amount of power is noted.

To validate the simultaneous uplink and downlink communication capability, two NFM signals (Signal-I with a 20 MHz bandwidth and Signal-II with a 15 MHz bandwidth) are generated using SDRangle. Signal-I is transmitted through SDR-1 using Port-1 of the duplex antenna, while Signal-II is transmitted through the external antenna (Dipole-3) of SDR-3. The external antenna (Dipole-4) receives Signal-I from the duplex antenna, and Port-2 of the duplex antenna receives Signal-II from the external antenna (Dipole-3). With this configuration, the simultaneous uplink and downlink capability of the proposed antenna is practically demonstrated, with Port-1 acting as the transmitter and Port-2 as the receiver.

To the best of the authors' knowledge, this design marks the introduction of the first IBFD implantable antenna in the literature. The proposed antenna design offers several advantages over existing implantable antennas, as evident from the comparison in Table IV. The elimination of the multiplexer enhances the antenna's compactness, resulting in the smallest footprint among the reported designs. Despite the ability of [16], [17] to communicate simultaneously without a multiplexer, this approach leads to less efficient spectrum utilization due to the use of multiple frequency bands. Additionally, this method may encounter increased interference from neighboring devices operating on adjacent frequency bands [18]–[20]. In contrast, the proposed IBFD antenna performs simultaneous uplink and downlink communication using a single frequency band, saving frequency spectrum and minimizing interferences with other wireless devices. Furthermore, the antenna achieves superior isolation between ports, enabling simultaneous signal transmission and reception.

IV. CONCLUSION

This study presents an ultra-compact implantable IBFD antenna at 2.4 GHz, for WCE applications. The antenna design integrates multiple semi-circular slots and shorting pins to minimize the antenna's footprint to a 7.17 mm³ (calculated as $\pi \times (3)^2 \times 0.254$ mm), which surpasses the compactness of state-of-the-art antennas. The antenna is simulated within a human body phantom at a depth of 50 mm, displaying nearly omnidirectional radiation patterns for each port. The measured gains are -24.4 dBi and -24.5 dBi for ports 1 and 2, respectively, with an isolation level better than 28 dB. This high isolation level is crucial for minimizing signal interference to ensure reliable bi-directional communication. Moreover, the SAR is thoroughly evaluated to meet safety standards. A prototype is tested within minced pork to mimic the realistic biological environment. The antenna system reliably maintains a link margin of at least 10 dB, enabling communication over distances of more than 8 meters. Experimental results show strong agreement with simulation predictions, thus validating the antenna's performance. The antenna system presents

compact size, low coupling levels between the ports, and the capability to transmit and receive signals simultaneously without a multiplexer. These attributes make the proposed antenna a promising candidate for WCE devices that require robust two-way communication capabilities.

REFERENCES

- [1] A. Iqbal, M. Al-Hasan, I. B. Mabrouk, and M. Nedil, "A compact implantable mimo antenna for high-data-rate biotelemetry applications," *IEEE Transactions on Antennas and Propagation*, vol. 70, no. 1, pp. 631–640, 2021.
- [2] A. Basir, Y. Cho, I. A. Shah, S. Hayat, S. Ullah, M. Zada, S. A. A. Shah, and H. Yoo, "Implantable and ingestible antenna systems: From imagination to realization [bioelectromagnetics]," *IEEE Antennas and Propagation Magazine*, vol. 65, no. 5, pp. 70–83, 2023.
- [3] A. Kiourti and K. S. Nikita, "Miniature scalp-implantable antennas for telemetry in the mics and ism bands: Design, safety considerations and link budget analysis," *IEEE Transactions on antennas and propagation*, vol. 60, no. 8, pp. 3568–3575, 2012.
- [4] X. Tang, H. Wong, Y. Long, Q. Xue, and K. Lau, "Circularly polarized shorted patch antenna on high permittivity substrate with wideband," *IEEE Transactions on Antennas and Propagation*, vol. 60, no. 3, pp. 1588–1592, 2011.
- [5] C. Liu, Y.-X. Guo, and S. Xiao, "Capacitively loaded circularly polarized implantable patch antenna for ism band biomedical applications," *IEEE transactions on antennas and propagation*, vol. 62, no. 5, pp. 2407–2417, 2014.
- [6] A. Lamkaddem, A. E. Yousfi, V. González-Posadas, and D. Segovia-Vargas, "Miniaturized dual band implantable antenna for implanted biomedical devices," *IEEE Access*, vol. 12, pp. 15 026–15 036, 2024.
- [7] U. Banerjee, A. Karmakar, A. Saha, and P. Chakraborty, "A cpw-fed compact monopole antenna with defected ground structure and modified parasitic hiltbert strip having wideband circular polarization," *AEU-International Journal of Electronics and Communications*, vol. 110, p. 152831, 2019.
- [8] H. Li, Y.-X. Guo, C. Liu, S. Xiao, and L. Li, "A miniature-implantable antenna for medradio-band biomedical telemetry," *IEEE Antennas and Wireless Propagation Letters*, vol. 14, pp. 1176–1179, 2015.
- [9] P.-L. Chi, R. Waterhouse, and T. Itoh, "Antenna miniaturization using slow wave enhancement factor from loaded transmission line models," *IEEE Transactions on antennas and propagation*, vol. 59, no. 1, pp. 48–57, 2010.
- [10] C. Liu, Y.-X. Guo, and S. Xiao, "A hybrid patch/slot implantable antenna for biotelemetry devices," *IEEE Antennas and Wireless Propagation Letters*, vol. 11, pp. 1646–1649, 2012.
- [11] M. Zada and H. Yoo, "A miniaturized triple-band implantable antenna system for bio-telemetry applications," *IEEE Transactions on Antennas and Propagation*, vol. 66, no. 12, pp. 7378–7382, 2018.
- [12] B. Joy, Y. Cai, D. C. Bono, and D. Sarkar, "Cell rover—a miniaturized magnetostrictive antenna for wireless operation inside living cells," *Nature Communications*, vol. 13, no. 1, p. 5210, 2022.
- [13] Y. Zhang, C. Liu, X. Liu, K. Zhang, and X. Yang, "A wideband circularly polarized implantable antenna for 915 mhz ism-band biotelemetry devices," *IEEE Antennas and wireless propagation letters*, vol. 17, no. 8, pp. 1473–1477, 2018.
- [14] S. Hayat, S. A. A. Shah, and H. Yoo, "Miniaturized dual-band circularly polarized implantable antenna for capsule endoscopic system," *IEEE Transactions on Antennas and Propagation*, vol. 69, no. 4, pp. 1885–1895, 2020.
- [15] S. Ding, S. Koulouridis, and L. Pichon, "Implantable wireless transmission rectenna system for biomedical wireless applications," *IEEE Access*, vol. 8, pp. 195 551–195 558, 2020.
- [16] A. Iqbal, M. Al-Hasan, I. B. Mabrouk, and T. A. Denidni, "Wireless powering and telemetry of deep-body ingestible bioelectronic capsule," *IEEE Transactions on Antennas and Propagation*, vol. 70, no. 10, pp. 9819–9830, 2022.
- [17] A. Iqbal, M. Al-Hasan, I. B. Mabrouk, A. Basir, M. Nedil, and H. Yoo, "Biotelemetry and wireless powering of biomedical implants using a rectifier integrated self-diplexing implantable antenna," *IEEE Transactions on Microwave Theory and Techniques*, vol. 69, no. 7, pp. 3438–3451, 2021.
- [18] S. Hashemi, S. Sarafan, and H. Cao, "Triple-band implantable antenna design for biotelemetry applications in mics/ism/wi-fi/bluetooth bands," *Technologies*, vol. 10, no. 4, p. 91, 2022.
- [19] F. Merli, "Implantable antennas for biomedical applications," *IEEE Transactions on Antennas and Propagation*, vol. 59, no. 10, pp. 3545–3553, 2011.
- [20] A. Sabharwal, P. Schniter, D. Guo, D. W. Bliss, S. Rangarajan, and R. Wichman, "In-band full-duplex wireless: Challenges and opportunities," *IEEE Journal on Selected Areas in Communications*, vol. 32, no. 9, pp. 1637–1652, 2014.
- [21] S. Gabriel, R. Lau, and C. Gabriel, "The dielectric properties of biological tissues: Iii. parametric models for the dielectric spectrum of tissues," *Physics in medicine & biology*, vol. 41, no. 11, p. 2271, 1996.
- [22] R. B. Waterhouse and R. Waterhouse, "Small microstrip patch antennas," *Microstrip Patch Antennas: A Designer's Guide*, pp. 197–276, 2003.
- [23] Z. Qamar, U. Naeem, S. A. Khan, M. Chongchewchamman, and M. F. Shafique, "Mutual coupling reduction for high-performance densely packed patch antenna arrays on finite substrate," *IEEE Transactions on Antennas and Propagation*, vol. 64, no. 5, pp. 1653–1660, 2016.
- [24] C. A. Balanis, *Antenna theory: analysis and design*. John Wiley & sons, 2016.
- [25] L. Chang, A. Iqbal, A. Basir, R. B. V. B. Simorangkir, and I. Ben Mabrouk, "Conformal mimo ultrawideband antenna design for high-speed wireless telemetry in capsule endoscopy systems," *IEEE Transactions on Antennas and Propagation*, vol. 72, no. 7, pp. 5724–5732, 2024.
- [26] A. Iqbal, S. H. Kiani, M. Al-Hasan, I. B. Mabrouk, and T. A. Denidni, "A compact dual-band implantable mimo antenna for wireless capsule endoscopy," *IEEE Transactions on Antennas and Propagation*, pp. 1–1, 2024.
- [27] W. H. Bailey, R. Bodemann, J. Bushberg, C.-K. Chou, R. Cleveland, A. Faraone, K. R. Foster, K. E. Gettman, K. Graf, T. Harrington *et al.*, "Synopsis of ieee std c95. 1™-2019 "ieee standard for safety levels with respect to human exposure to electric, magnetic, and electromagnetic fields, 0 hz to 300 ghz"," *IEEE Access*, vol. 7, pp. 171 346–171 356, 2019.
- [28] I. T. Union, "Recommendation ITU-R SM.2153-8," 2021, [Online]. Available: <https://www.itu.int/pub/R-REP-SM.2153-8-2021>.
- [29] M. Zada, I. A. Shah, and H. Yoo, "Metamaterial-loaded compact high-gain dual-band circularly polarized implantable antenna system for multiple biomedical applications," *IEEE Transactions on Antennas and Propagation*, vol. 68, no. 2, pp. 1140–1144, 2019.
- [30] Z. Duan and L.-j. Xu, "Dual-band implantable antenna with circular polarisation property for ingestible capsule application," *Electronics Letters*, vol. 53, no. 16, pp. 1090–1092, 2017.
- [31] A. Alshammari, A. Iqbal, A. Basir, R. B. V. B. Simorangkir, and I. B. Mabrouk, "Ultraminiaturized dual-band implantable antenna for wireless capsule endoscopy," *IEEE Sensors Journal*, vol. 24, no. 9, pp. 15 210–15 218, 2024.
- [32] I. A. Shah, M. Zada, and H. Yoo, "Design and analysis of a compact-sized multiband spiral-shaped implantable antenna for scalp implantable and leadless pacemaker systems," *IEEE Transactions on Antennas and Propagation*, vol. 67, no. 6, pp. 4230–4234, 2019.
- [33] A. Basir, M. Zada, Y. Cho, and H. Yoo, "A dual-circular-polarized endoscopic antenna with wideband characteristics and wireless biotelemetric link characterization," *IEEE Transactions on Antennas and Propagation*, vol. 68, no. 10, pp. 6953–6963, 2020.
- [34] M. Zada and H. Yoo, "Miniaturized dual band antennas for intra-oral tongue drive system in the ism bands 433 mhz and 915 mhz: Design, safety, and link budget considerations," *IEEE transactions on antennas and propagation*, vol. 67, no. 9, pp. 5843–5852, 2019.
- [35] Y. Liu, Y. Chen, H. Lin, and F. H. Juwono, "A novel differentially fed compact dual-band implantable antenna for biotelemetry applications," *IEEE Antennas and Wireless Propagation Letters*, vol. 15, pp. 1791–1794, 2016.
- [36] J. Zhang, R. Das, D. Hoare, H. Wang, A. Ofiare, N. Mirzai, J. Mercier, and H. Heidari, "A compact dual-band implantable antenna for wireless biotelemetry in arteriovenous grafts," *IEEE Transactions on Antennas and Propagation*, vol. 71, no. 6, pp. 4759–4771, 2023.



Citation on deposit:

Alshammari, A., Iqbal, A., Basir, A., Al-Hasan, M., Simorangkir, R. B. V. B., Nedil, M., & Mabrouk, I. B. (2024). Compact In-Band Full-Duplex Implantable Antenna for Wireless Capsule Endoscopy. IEEE

Transactions on Antennas and Propagation, 1-1.

<https://doi.org/10.1109/tap.2024.3499367>

For final citation and metadata, visit Durham Research Online URL:

<https://durham-repository.worktribe.com/output/3201970>

Copyright Statement:

This accepted manuscript is licensed under the Creative Commons Attribution 4.0 licence. <https://creativecommons.org/licenses/by/4.0/>